Boundary crossing in epithelial wound healing

Eileen Fong[a,1], Shelly Tzlil[b,1], and David A. Tirrell[b,c,2]

[a]Department of Bioengineering, [b]Division of Chemistry and Chemical Engineering, and [c]Joseph J. Jacobs Institute for Molecular Engineering for Medicine, California Institute of Technology, Pasadena, CA 91125

The processes of wound healing and collective cell migration have been studied for decades. Intensive research has been devoted to understanding the mechanisms involved in wound healing, but the role of cell-substrate interactions is still not thoroughly understood. Here we probe the role of cell-substrate interactions by examining in vitro the healing of monolayers of human corneal epithelial (HCE) cells cultured on artificial extracellular matrix (aECM) proteins. We find that the rate of wound healing is dependent on the concentration of fibronectin-derived (RGD) cell-adhesion ligands in the aECM substrate. The wound closure rate varies nearly sixfold on the substrates examined, despite the fact that the rates of migration and proliferation of individual cells show little sensitivity to the RGD concentration (which varies 40-fold). To explain this apparent contradiction, we study collective migration by means of a dynamic Monte Carlo simulation. The cells in the simulation spread, retract, and proliferate with probabilities obtained from a simple phenomenological model. The results indicate that the overall wound closure rate is determined primarily by the rate at which cells cross the boundary between the aECM protein and the matrix deposited under the cell sheet.

biomaterials | integrins | elastin

The collective migration of cells is fundamental to wound healing, morphogenesis, and many bioengineering applications. Wound healing in particular involves the migration of cell sheets over adhesive surfaces. Two mechanisms of migration have been identified in wound healing (1). First is the "purse string" mechanism in which a marginal actomyosin cable develops along the wound edge, and wound closure proceeds with contraction of the actin belt (2). The second mechanism involves active spreading and migration of cells at the wound edge, known commonly as "lamellipodial crawling." The latter mechanism is more frequently observed in vitro and has been characterized by using scratch-wound models. In these models, cells experience an injury, which triggers cell migration through various biochemical signaling events (3). It has also been argued that the availability of free space is sufficient to initiate cell migration in the absence of mechanical injury (4–6). Upon wounding, proliferation is up-regulated (7).

Adhesive cell-substratum interactions are required for sustained migration into the wound area (8, 9). The rates of migration of individual cells are governed by surface adhesivity in a biphasic fashion, at least under certain conditions (10). Surfaces modified with adhesion ligands such as fibronectin (FN) (11–13) and Arg-Gly-Asp (RGD) peptides have been shown to facilitate wound healing, and it is reasonable to infer that the observed increases in healing rates arise primarily from faster migration of individual cells. We show here that other factors can be more important.

The substrates used in this work were prepared from artificial extracellular matrix (aECM) proteins that combine domains derived from fibronectin and elastin (Fig. S1). We and others have shown that such aECM proteins can be cross-linked to yield materials with elastic moduli similar to those of natural elastins (14, 15) and that presentation of the fibronectin-derived RGD sequence promotes cell spreading and adhesion (16–18).

Wound healing was examined in monolayers of human corneal epithelial cells (HCE) cultured on aECM protein substrates that present controlled, varying densities of the RGD sequence. HCE cells undergo rapid reepithelization in vivo (19). Both the $\alpha_5\beta_1$ and $\alpha_v\beta_3$ integrins, which bind RGD, are up-regulated by wounding (20). Cross-linked films with estimated RGD surface densities varying from 7.7×10^3 to 3.1×10^5 per μm^2 were prepared by mixing aECM proteins containing RGD and "scrambled" (RDG) domains (see SI Text). Substrates are identified by specifying the percentage of the RGD protein in the film (e.g., 100% RGD).

Results and Discussion

Cell Spreading. HCE cells were allowed to spread on spin-coated aECM films containing varying RGD densities. After 4 h, HCE cells were well-spread on cross-linked 100% RGD and on adsorbed FN but remained rounded on the scrambled control (0% RGD) and on adsorbed BSA surfaces (Fig. 1 A–D). To quantify these differences, projected areas of 250 cells were measured at each of several time points over a 4-h period. Cells with projected areas larger than 300 μm^2 were considered well-spread. The percentage of well-spread cells on aECM films increased with RGD density (Fig. 1E). Although some cells eventually spread on the scrambled control substrate, spreading on the control surface was likely a consequence of cellular secretion of ECM proteins (21, 22).

Wound Healing. Conventional scratch-wound assays are of limited use in studies of cell-substrate interactions because of interference from proteins deposited by cells removed from the wound. Nikolić et al. (6) and others (4) have shown that removal of a PDMS barrier triggers cell responses similar to those observed in scratch-wound assays. Using a similar approach, we precoated glass coverslips with the protein of interest and laid down a short PDMS slab to provide a temporary platform for cell attachment. To facilitate cell attachment, fibronectin was incubated in each well overnight prior to plating of HCE cells (Fig. 2A). Removal of the PDMS slab placed the edge of the wounded cell sheet in contact with the test surface. HCE cells migrated collectively in the direction of the wound by lamellipodial crawling on 100% RGD, consistent with previous reports (5, 23). On 2.5% RGD, however, minimal advance of the cell sheet was observed, even though cells at the wound edge were constantly extending protrusions (Fig. 2B and Movies S1–S6). Fig. 3A shows the average displacement of the cell sheet on various surfaces as a function of time. The overall wound closure rate increases approximately 5.6-fold as the RGD density increases (Fig. 3B and Table S1). Individual cells within the cell sheet were also tracked for the last 10 h of each video (Fig. 3C). Cells were selected at random and only cells on the test surface were included in the analysis.
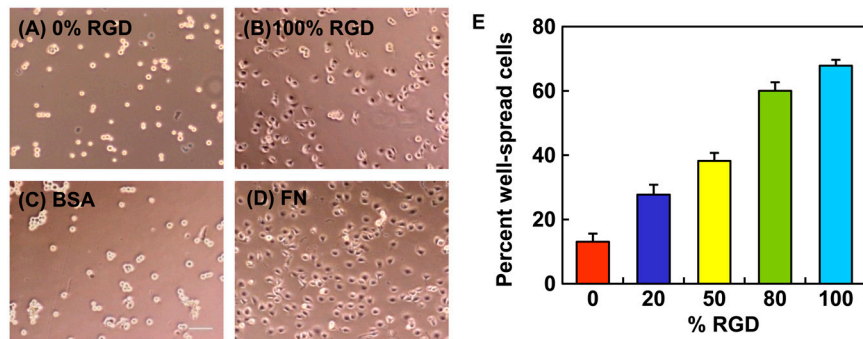
Fig. 1. HCE cell spreading behavior. Phase contrast images of HCE cells after 4 h on cross-linked spin-coated aECM films prepared from 0% RGD (*A*) or 100% RGD (*B*), adsorbed bovine serum albumin (BSA) (*C*) and adsorbed fibronectin (FN) (*D*). Scale bar, 100 μm. (*E*) Percent well-spread cells after 4 h on spin-coated aECM films with varying RGD densities. Error bars represent SEM.

Surprisingly, cells migrated just 40% faster on 100% RGD than on 2.5% RGD.

This result was puzzling—we expected the increase in wound closure rate with RGD concentration to be a consequence of an increase in cell speed. But a 1.4-fold increase in cell speed cannot explain the observed 5.6-fold increase in wound closure rate. We considered the possibility that differences in proliferation rates might provide an explanation, so we determined the fraction of cells in the wound area that arose through cell division. We found that even on the most highly adhesive surfaces, proliferation provided no more than 15% of the cells in the wound area (Fig. S7*B* and Table S2). Variation in proliferation rates therefore cannot account for large differences in the rates of wound closure. Finally, we imagined that a critical event might be the "decision" made by each cell as it comes into contact with the test surface. Does the cell cross to the test surface or retreat to the matrix deposited beneath the confluent cell monolayer? If the rate of crossing increases with the adhesivity of the test surface, wound healing should occur more rapidly on surfaces bearing higher RGD densities. By counting cells in the wound area after 30 h and subtracting proliferation events, we estimated that boundary crossing contributes approximately 4.3-fold more cells to wound healing on 100% RGD than on 2.5% RGD (Fig. S7*D* and Table S2). In order to gain additional insight into the various factors that determine the wound-healing rate, we performed computer simulations of the healing process.

Dynamic Monte Carlo simulation. The surface was modeled as a 2D hexagonal lattice in which each lattice site was either occupied by a cell or empty. Cell migration in the simulation proceeds via a two-step mechanism: First, the cell spreads onto an adjacent lattice site, and then it retracts to a single lattice site (Fig. 2*C*).
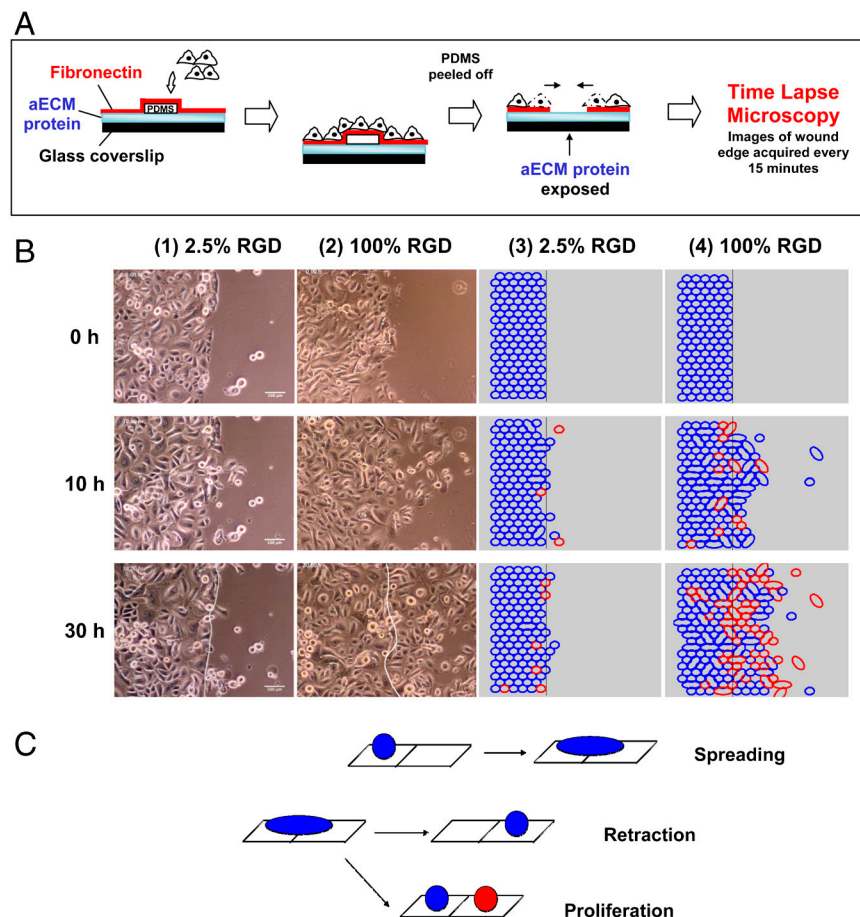
Fig. 2. (*A*) Schematic of wound-healing experiment. aECM proteins were spin-coated and cross-linked on glass coverslips and mounted in multiwell tissue culture plates. A slab of PDMS was laid on top of the protein film and fibronectin solution was allowed to adsorb overnight at 4 °C to aid cell attachment. HCE cells were grown to confluence and the PDMS was peeled off. The protein film was rinsed twice with serum-free medium and the wounded cell sheet was allowed to migrate over the aECM protein. This process was monitored by time-lapse microscopy. (*B*) Time course of wound healing on 2.5% RGD and 100% RGD substrates. (Panels **1** and **2**) Experimental images showing the progression of the wound edge on 2.5% and 100% RGD, respectively, at various time intervals. (Panels **3** and **4**) Snapshots of simulated wound edges for 2.5% RGD and 100% RGD substrates. "Daughter cells" are shown in red. The initial positions of the wound edge are indicated by white lines in the images at 30 h. (*C*) Schematic of the Monte Carlo simulation. In the model, cells can spread with probability W_s to take up two lattice sites, retract to either one of the sites with probability W_r, or undergo proliferation with probability W_p. Following each proliferation event, the daughter cell is colored red; thus the number of red cells corresponds to the contribution of proliferation to cell number. The decision regarding which cell is the daughter and which cell is the "mother" was made by generating a random number.

Fong et al.
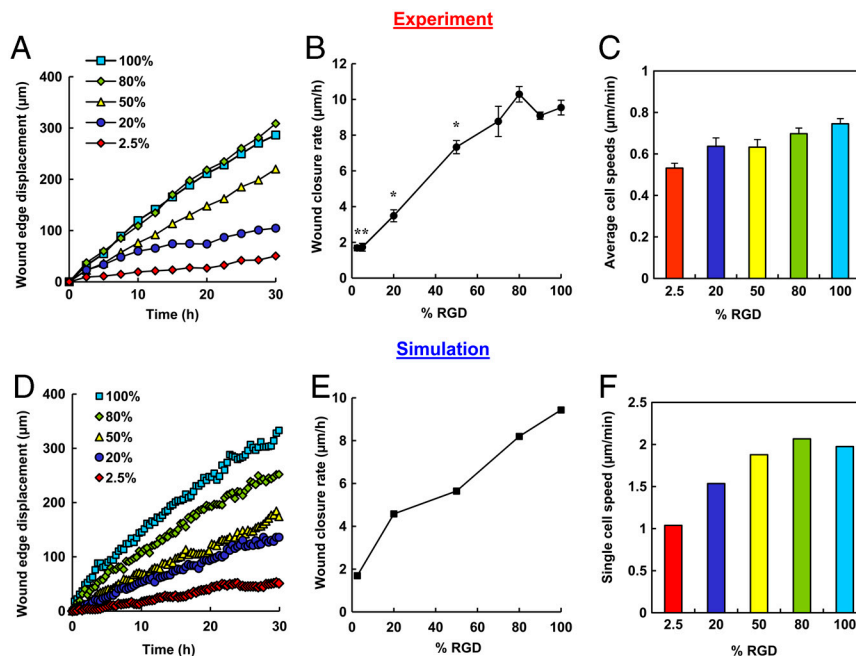
Fig. 3. Wound-healing behavior observed in experiments (*A–C*) and simulations (*D –F*). (*A*) Displacement of the wound edge for various surfaces over time. (*B*) Wound closure rate for substrates with varying RGD densities. *, significant difference from 100% RGD ($P < 0.05$). (*C*) Average speeds for individual cells migrating on the test surface for the last 10 h. (*D*) Displacement of simulated wound edges as a function of time. (*E*) Wound-closure rate as a function of RGD percentage. The wound-closure rate is fivefold faster on 100% RGD than on 2.5% RGD, consistent with experimental observations. (*F*) Single cell speed as a function of RGD concentration. Only cells on the test surface were included. Error bars represent SEM.

If retraction vacates the site occupied by the cell before it spread, migration has occurred.

We define the *x*-axis as the axis perpendicular to the wound edge, and the initial position of the wound edge (the boundary) as $x = 0$. Thus, in the initial configuration of the simulation, cells occupy all the lattice sites whose *x* positions are smaller than zero, and the rest of the sites are empty. As the simulation progresses, cells cross the boundary into the wound area, and the value of *x* at the wound edge position increases. We denote the transition probabilities for spreading, retraction, and proliferation by W_s, W_r, and W_p, respectively. We use a simple model for spreading and retraction behavior to estimate the values of W_s and W_r for the different surfaces, based on experimental data. Because FN is a major component of the matrix deposited beneath the confluent monolayer, the probabilities for spreading and retraction for lattice sites with $x < 0$ were taken to be those for FN. We estimated the proliferation rate (W_p) by constructing rate equations according to the simulation rules and solving them in the low cell concentration limit. The doubling time was then compared to experimental data.

The cells in the simulation behaved similarly to those observed experimentally, in the dynamic nature of their bonds and in the difference in cell behaviors observed on surfaces that present different densities of RGD ligands. Fig. 2*B* compares snapshots taken from the simulation and from experiments for the 100% and 2.5% RGD surfaces. The wound closure rates derived from the simulation are shown in Fig. 3*E*. The wound closure rate is defined as the average distance traveled by the wound edge per unit time (Fig. 3*D*). As observed experimentally, there is a 5.6-fold difference between the wound closure rates on the 100% and on 2.5% RGD surfaces. Fig. 3*F* shows the single cell speeds calculated from the simulation for surfaces bearing various RGD densities. At each time point, only cells on the test surface were included in the analysis. The difference between the single cell speeds on 100% RGD and 2.5% RGD is only 1.9-fold. These observations are consistent with the experimental results and

confirm that the increase in overall wound closure rate does not require faster cell migration.

The Variation in Wound-Closure Rate Is Determined Primarily by the Rate of Boundary Crossing. The probability that a cell crosses the matrix boundary is given by its probability to spread onto the RGD test surface multiplied by its probability to retract from the FN surface, i.e., $W_s^{\mathrm{RGD}} \times W_r^{\mathrm{FN}}$. Hence, the ratio of the probabilities for crossing to the 100% RGD and 2.5% RGD test surfaces is: $P_{\mathrm{FN}\to100\%\mathrm{RGD}}/P_{\mathrm{FN}\to2.5\%\mathrm{RGD}} = W_s^{100\%\mathrm{RGD}}/W_s^{2.5\%\mathrm{RGD}} = 5.3$. The second equality was obtained from the spreading rates used in the simulation. We used the cell spreading assay data (Fig. 1*E*) to determine these rates (see additional details in *SI Text*). Hence, the 5.3-fold difference in crossing probability arises from the 5.3-fold difference in the rate of cell spreading. Following the same logic, we can also explain the small differences in cell speed observed in the simulation for surfaces with different RGD concentrations. The ratio between single cell migration rates on 100% and 2.5% RGD is $W_s^{100\%\mathrm{RGD}} \times W_r^{100\%\mathrm{RGD}}/W_s^{2.5\%\mathrm{RGD}} \times W_r^{2.5\%\mathrm{RGD}} = 1.8$. The simulation results suggest that the 5.6-fold variation in wound-closure rates observed experimentally arises primarily from variation in boundary-crossing rates (Fig. 4*B* and Fig. S6*B*).

To measure boundary-crossing rates directly, we prepared substrates by spin-coating one layer of aECM protein on top of another (Fig. S2). Single HCE cells were seeded on these surfaces, and cells at the boundary were followed by time-lapse microscopy (see Movies S1–S6). The total time in contact with the boundary and the subsequent decision (i.e., to cross the boundary or not) were recorded for each cell. The crossing rate was calculated by dividing the number of crossings by the total time in contact with the boundary. The results confirm that the crossing rate increases 5.7-fold as the adhesivity of the substrate increases (Fig. 4*C*), consistent with the hypothesis that the variation in wound-closure rate is determined primarily by variation in the rate of boundary crossing.
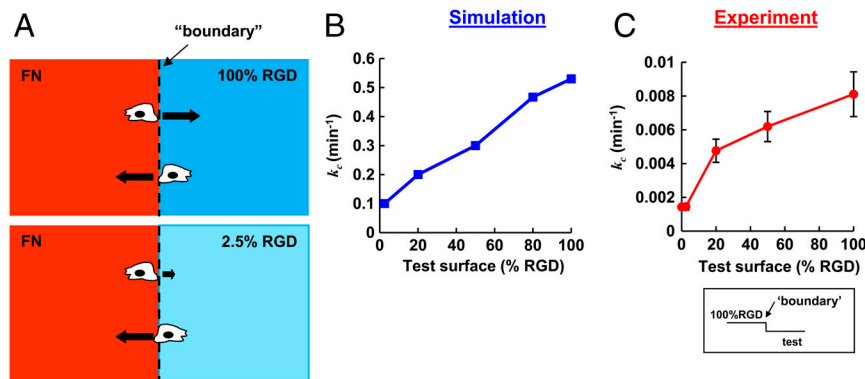
Fig. 4. (*A*) Schematic representation of boundary crossing. Black arrows represent relative crossing rates for each condition. *B* and *C* show the rate constants of crossing, k_c (from 100% RGD to the test surfaces), for simulation and experimental data, respectively. In both curves, the crossing rates from 100% RGD to 100% RGD and from 100% RGD to 2.5% RGD differ by a factor of five. Error bars in *C* are experimental errors (see *SI Text*).

Concluding Remarks

In summary, we find that the rate of healing of epithelial cell monolayers cultured on aECM proteins increases with increasing density of adhesion ligands presented at the substrate surface. As shown both experimentally and through simulation of the healing process, the variation in healing rate arises primarily from variation in the rate at which cells cross the boundary between the matrix deposited by the cell monolayer and the aECM protein; variation in the rates of migration and proliferation play comparatively minor roles. The simulation method described here can be applied to many cell types, and—through variation in the cell–cell interaction energy (see *SI Text*)—captures a broad range of wound-healing behavior, from diffusion-like behavior in which cell–cell contacts break and reform (as observed for corneal epithelial cells) to behavior that resembles that of an elastic sheet in which cell–cell contacts remain unchanged during wound healing (as observed in monolayers of MDCK cells) (24).

Materials and Methods

Protein Expression and Purification. Standard methods for cloning, bacterial growth, protein expression, sodium dodecyl sulfate-polyacrylamide gel electrophoresis (SDS/PAGE), and Western blotting were used to prepare and characterize aECM proteins containing RGD and RDG domains (17). Typical yields of protein obtained from 10 L fermentation cultures were approximately 500 mg. The molar mass of each aECM protein was 34.8 kDa.

Preparation of Spin-Coated aECM Films. Round glass coverslips (12 mm diameter; No. 1, Deckgläser) were sonicated in a mixture of ethanol and KOH for 15 min and rinsed several times with distilled H_2O. aECM protein solutions were prepared by dissolving mixtures of aECM-RGD and aECM-RDG (100 mg/ml in ddH$_2$O) for 3–4 h at 4 °C. Protein solutions containing 2.5%, 5%, 20%, 35%, 50%, 70%, 75%, 80%, 90%, and 100% aECM-RGD were prepared. Bis[sulfosuccinimidyl]suberate (BS³) was used to cross-link the aECM protein substrates. BS³ (2.0 mg; Pierce) was dissolved in 17 μl of sterile distilled H_2O and added to 150 μl of protein solution, mixed and centrifuged to remove bubbles. The stoichiometric ratio of activated esters in BS³ to primary amines in the aECM proteins was roughly 1:1. A 17 μl volume of BS³-protein solution was then spin-coated on a 12 mm diameter round glass cover slip at 7,000 rpm for 30 sec at 4 °C. Each protein film was stored overnight at 4 °C before use.

Generation of aECM Films Containing Boundaries. We prepared 100 μl of aECM protein solutions (25 mg/ml in distilled H_2O) containing 0%, 2.5%, 20%, 50%, and 100% aECM-RGD and BS³ (0.29 mg in 2.5 μl ddH$_2$O) as previously described. The protein solution (17 μl) was spin-coated onto a 12 mm diameter round glass coverslip at 5,000 rpm 30 sec at 4 °C. Protein films were allowed to dry overnight at 4 °C. Subsequently, 600 μl of a second aECM protein solution (15 mg/ml) was mixed with 1.725 mg of BS³ dissolved in 12.75 μl distilled H_2O. A small volume (2 μl) of the second aECM protein solution was pipetted across the middle of the film and spin-coated at 5,000 rpm for 30 sec at 4 °C. Under these conditions, a boundary was generated between two distinct aECM surfaces.

Wound-Healing Assay. The experimental set up was adapted from Nikolic et al. with modifications (6). Slabs of polydimethylsiloxane (PDMS; Sylgard 184, Dow Corning) were cast to 0.3 mm thickness according to the manufacturer's instructions. Briefly, PDMS was mixed at 10:1 PDMS base/curing agent ratio, poured into a 100 mm Petri dish to a height of 0.3 mm, degassed in a desiccator for at least 1 h and baked for at least 2 h at 65 °C. Slabs of PDMS with lateral dimensions roughly 2 mm*x*2 mm were cut with a sterile scalpel, sterilized with ethanol and air-dried. Use of thin (0.3 mm) blocks of PDMS allowed cells to maintain confluence across the edge of the slab and prevented contact between cells and the underlying substrate surface. The PDMS slabs were placed at the center of the coverslips containing spin-coated aECM films. These coverslips were then mounted in 24-well tissue culture plates by using sterile vacuum grease (Dow Corning). To all wells, 500 μl of FN was added overnight at 4 °C to cover the entire surface to aid cell-adhesion. The next day, 2×10^5 primary HCE cells were seeded into each well and allowed to grow to confluence over 3–5 d. The medium was changed every 2 d. Once a confluent monolayer formed, the PDMS slabs were lifted with sterile tweezers to create a wounded cell sheet. A schematic drawing of the experimental set up is shown in Fig. 2*A*. Each well was rinsed twice with fresh medium before the start of each experiment to remove any cell debris. Meanwhile, a chamber was set up around the microscope to maintain the microscope stage and chamber interior at 37 °C with 5% CO_2/95% air to sustain cells. A hole was opened in the cover of one of the empty wells in the 24-well plate and an air supply was attached to ensure that cells were maintained under the CO_2/air mixture. Water was also added to surrounding empty wells to prevent excessive evaporation of the medium. Wound closure was followed for 30 h by time-lapse phase contrast microscopy on a Nikon Eclipse TE300 microscope at 10 × magnification. Digital images of at least 5 different spots of the wound edge for each substrate were acquired every 15 min using MetaMorph v6.3.2 (Molecular Devices). The wound areas immediately after wounding ($t = 0$ h) and after 30 h ($t = 30$ h) were traced manually using ImageJ v1.37 (NIH, http://rsb.info.nih.gov/ij/). The difference in the two areas was then divided by the length of the wound edge to yield the distance traveled by the cell sheet. This distance was then divided by the total time (30 h) to give the wound-closure rate. The reported wound-closure rates were obtained by averaging the rates calculated from videos recorded in at least three independent experiments. Individual cells within the sheet were also tracked manually with ImageJ, with MTrackJ, a plug-in created by Meijering and colleagues at the University Medical Center Rotterdam, Netherlands (http://www.bigr.nl/). Trajectories of individual cells were tracked frame by frame for the last 10 h for each video and the average speeds of individual cells were averaged for all cells migrating on the test surface. The extent to which proliferation on the test surface contributed to wound closure was quantified by counting the number of proliferation events on the test surface and comparing that number to the total number of cells on the test surface at the end of the experiment. The number of cells that crossed the boundary was calculated by counting the number of cells on the test surface at the end of the experiment and subtracting the number of cells that result of proliferation (subtracting the number of proliferation events on the test surface).

Modeling Spreading, Retraction, and Proliferation. We use a simple phenomenological model to estimate numerical values for the rates of cell spreading, retraction, and proliferation. As shown in Fig. 5, the cell membrane is modeled as a chain of beads that represent integrin receptors or clusters, and

Fong et al.
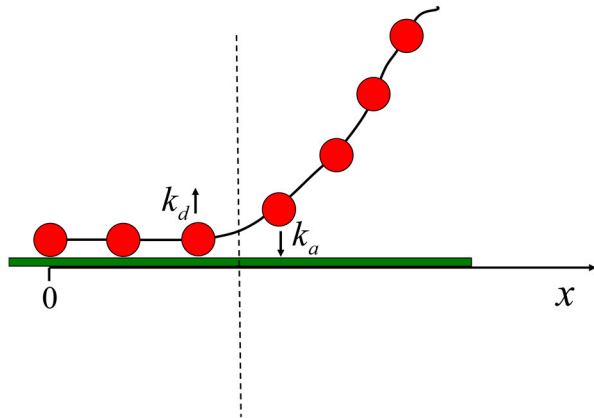
Fig. 5. Schematic illustration of the cell spreading and retraction model. The beads represent integrin receptor clusters, while the chain represents the cell membrane. The cell edge is represented by the dashed line. Receptor clusters adjacent to the cell edge can adsorb or desorb with rate constants k_a and k_d, respectively.

spreading and retraction involve adsorption and desorption of receptor clusters at the ligand-bearing surface. Only the receptor clusters adjacent to the cell edge (which is represented by the dashed line in Fig. 5) can adsorb or desorb. The rate constants for adsorption and desorption are k_a and k_d, respectively. During spreading and retraction, the cell edge performs a random walk where each adsorption event results in an increase in its x position while each desorption event results in a decrease in its x position.

The master equation that describes the processes discussed above is of the form

$$\frac{dP(x,t)}{dt} = k_a P(x-1,t) + k_d P(x+1,t) - (k_a + k_d)P(x,t) \quad [1]$$

where $P(x,t)$ is the probability of the cell edge to be at position x at time t, and x is measured in units equal to the average distance between receptor clusters. The solution for the average cell edge displacement is

$$\langle x \rangle = (k_a - k_d) \cdot t. \quad [2]$$

An increase in $\langle x \rangle$ corresponds to an increase in the cell area in contact with the surface. Therefore, we define the spreading rate, W_s, as the change in the average value of x with time

$$W_s = \frac{d\langle x \rangle}{dt} = (k_a^s - k_d^s). \quad [3]$$

Similarly, the retraction rate, W_r, is defined as

$$W_r = -\frac{d\langle x \rangle}{dt} = (k_d^r - k_a^r). \quad [4]$$

The forces exerted by the cell influence the effective rate of receptor adsorption and desorption events (k_a and k_d). Because the forces exerted by the cell differ depending on whether the cell is spreading or retracting, the rate constants for adsorption and desorption in these two cases will be different. Consequently, we add a superscript in Eqs. 3 and 4 (s or r) to denote the cell state (spreading or retraction).

In a cell-free system with receptors incorporated into a rigid planar membrane, the binding of the receptors to surface ligands can be described as a second order reaction. Denoting the rate constant for binding by k and the rate constant for unbinding by k_{-1}, the ratio of these rate constants is $k_{-1}/k = \exp(-\varepsilon/k_B T)$ where $\varepsilon > 0$ is the binding energy (the difference in energy between the unbound and bound states).

For the case of a flexible cell membrane, the spreading process is associated with a change in membrane shape. The shape deformation results in an energy barrier that we denote by ε_{el}. Spreading and retraction processes are not spontaneous and require forces to be generated by the cell (25). In the case of spreading, a protrusive force is exerted on the cell membrane and reduces the energy barrier associated with membrane deformation by an amount $f\gamma$ where f is the force applied by the cell and γ is the distance over

which the force is applied (10, 26). In this case the rate constants for adsorption and desorption in our model are

$$k_a^s = k \exp(-\varepsilon_{el}/k_B T + f\gamma/k_B T), \qquad k_d^s = k \exp(-\varepsilon/k_B T). \quad [5]$$

When retracting, the cell pulls on the receptor–ligand bond, thereby reducing the energy barrier associated with bond breakage by an amount $f'\gamma'$ (25–26).

In this case, the rate constants take the form

$$k_a^r = k \exp(-\varepsilon_{el}/k_B T), \qquad k_d^r = k \exp(-\varepsilon/k_B T + f'\gamma'/k_B T). \quad [6]$$

Following Eqs. 3–6, the rates for spreading and retraction can be expressed as

$$W_s = k \exp(-\varepsilon_{el}/k_B T + f\gamma/k_B T) - k \exp(-\varepsilon/k_B T) \quad [7]$$

$$W_r = k \exp(-\varepsilon/k_B T + f'\gamma'/k_B T) - k \exp(-\varepsilon_{el}/k_B T). \quad [8]$$

Using Eqs. 7 and 8, we can connect the spreading and retraction rates on surfaces with the same RGD fraction, φ_{RGD}:

$$\tilde{W}_r(\varphi_{RGD}) = \exp(f'\gamma'/k_B T)[A - \tilde{W}_s(\varphi_{RGD})] \\ - k \exp(-\varepsilon_{el}/k_B T)/W_s(FN). \quad [9]$$

In Eq. 9, $W_s(FN)$ denotes the spreading rate on fibronectin, $\tilde{W}_s(\varphi_{RGD}) = W_s(\varphi_{RGD})/W_s(FN)$ and $\tilde{W}_r(\varphi_{RGD}) = W_r(\varphi_{RGD})/W_s(FN)$ are the spreading and retraction rates relative to the spreading rate on fibronectin and $A \equiv k \exp(-\varepsilon_{el}/k_B T + f\gamma/k_B T)/W_s(FN)$. We can use the results from the spreading assay (Fig. 1E) in order to get a numerical value for the constant A (see *SI Text* for details).

The rest of the model parameters were estimated on the basis of experimental results described in the literature:

1. γ is the characteristic distance between bonds that link the cell and the substrate (the distance between beads in our model) and is estimated to be 100 nm (27).
2. The characteristic traction force is assumed in the literature to be on the order of 1 nN/μm^2 (10, 28, 29) and the protrusion has a typical diameter of 0.1 μm (29), comparable to the average distance between bonds (27). These estimates lead to a traction force, f', on the order of 8 pN. The RGD–integrin bond length, γ', is on the order of 1 nm (10, 26).
3. Recent estimates suggest that the thermal deformation of the membrane is on the order of 5–10 nm (29, 30) implying that the energy required for deformation on the scale of the distance between bonds (~100 nm) cannot be provided by thermal fluctuations. Consequently, we assume that the term $\exp(-\varepsilon_{el}/k_B T)$ in Eq. 9 is negligible.

The rates of spreading and retraction in the simulation are normalized by the rate of spreading on FN, i.e., the values used in the simulation are $\tilde{W}_s$ and $\tilde{W}_r$, respectively. When a cell retracts, it either has to break the bonds with its neighbors or "pull" its neighbors along. Thus, the final expression for the retraction rate depends on the cell–cell interaction energy (see *SI Text* for details). For each RGD concentration, φ_{RGD}, the spreading rate, $\tilde{W}_s(\varphi_{RGD})$, was taken from the experimental data presented in Fig. S3. The value for the retraction rate on the same surface, $\tilde{W}_r(\varphi_{RGD})$ was calculated using Eq. 9.

The proliferation rate was calculated using

$$W_p = \frac{\ln 2}{t_D}(1 + W_r/W_s) \quad [10]$$

where t_D is the doubling time for human corneal epithelial (HCE) cells (for derivation of Eq. 10, see *SI Text*). Using the values for W_r and W_s on FN and $t_D = 25$ h (31), we get $W_p = 0.05$ h^{-1}. We assume that W_p is identical on all surfaces.

Dynamic Monte Carlo Simulation. We use a dynamic Monte Carlo scheme (32–33) to simulate the dynamics of collective cell migration. The surface is modeled as a 100×100 hexagonal lattice with a lattice constant of $d = 50$ μm, which is on the order of a cell diameter. At time $t = 0$, the first 10 columns of the lattice are occupied by cells (total number of cells,

$N = 1{,}000$), while the rest of the lattice sites are empty. Because proliferation is enabled, N increases with time. In every Monte Carlo step, N cells are chosen randomly and an attempt is made to change their state according to the appropriate rates for spreading, retraction, and proliferation ($\tilde{W}_s$, $\tilde{W}_r$, and W_p, respectively). All the rates in the simulation are scaled to ensure that the time steps are small enough so that in any Monte Carlo (MC) step only one event can occur. The interaction energy between nearest neighbor cells in the simulation is $\varepsilon_{\text{cell-cell}}/k_B T_{\text{eff}} = 0.7$ (for details see *SI Text*). The conversion between simulation time and experimental time was done by a one-time calibration, equating the wound-closure rates obtained from simulation and experiment for the 2.5% RGD substrate. By using this approach, we find that 1 MC step corresponds to 0.15 min and $W_s(FN) = 0.54$ min^{-1}.

Boundary-Crossing Experiments. aECM surfaces containing substrate boundaries were mounted into the wells of a 24-well tissue culture plate. HCE cells (1×10^4) were added to each well and allowed to attach for 2 h at 37 °C under 5% CO_2/95% air. Images of the boundary at several positions on the aECM film were acquired every 15 min for 24 h, by using phase contrast microscopy at 37 °C under 5% CO_2/95% air. Time-lapse videos were analyzed using ImageJ. We tracked cells that contacted the boundary and recorded the time spent at the boundary before a "decision" was made (i.e., the cell crossed the boundary or moved away). We considered each encounter a separate "event" (i.e., once the cell leaves the boundary and recontacts the boundary again, the timing restarts). The total amount of time spent at the boundary, t_{total}, the total number of events, N, and the total number of cells that sub-

sequently decide to cross the boundary, N_c, were recorded for at least 150 events for each condition. The rate constant of boundary crossing, k_c, was calculated using

$$k_c = \frac{N_c}{t_{\text{total}}} \tag{11}$$

(see *SI Text* for a derivation of Eq. **11**).

The uncertainty in the rate constant for boundary crossing is $k_c \Delta t / \langle t \rangle$ where $\langle t \rangle = t_{\text{total}}/N$ is the average waiting time at the boundary and Δt is the 15-min time interval between two consecutive time-lapse images.

Statistical Analysis. For all experimental data, the statistical significance of differences was estimated by analysis of variance followed by the Tukey test. Differences were taken to be significant at $P \leq 0.05$.

1. Martin P, Lewis J (1992) Actin cables and epidermal movement in embryonic wound healing. *Nature* 360:179–183.
2. Bement WM, Forscher P, Mooseker MS (1993) A novel cytoskeletal structure involved in purse string wound closure and cell polarity maintenance. *J Cell Biol* 121:565–578.
3. Sammak PJ, Hinman LE, Tran POT, Sjaastad MD, Machen TE (1997) How do injured cells communicate with the surviving cell monolayer? *J Cell Sci* 110:465–475.
4. Poujade M, et al. (2007) Collective migration of an epithelial monolayer in response to a model wound. *Proc Natl Acad Sci USA* 104:15988–15993.
5. Block ER, Matela AR, SundarRaj N, Iszkula ER, Klarlund JK (2004) Wounding induces motility in sheets of corneal epithelial cells through loss of spatial constraints. Roles of heparin-binding epidermal growth factor-like signaling. *J Biol Chem* 279:24307–24312.
6. Nikolic DL, Boettiger AN, Bar-Sagi D, Carbeck JD, Shvartsman SY (2006) Role of boundary conditions in an experimental model of epithelial wound healing. *Am J Physiol-Cell Ph* 291:C68–C75.
7. Todaro GJ, Lazar GK, Green H (1965) The initiation of cell division in a contact-inhibited mammalian cell line. *J Cell Physiol* 66:325–333.
8. Suzuki K, et al. (2003) Cell-matrix and cell-cell interactions during corneal epithelial wound healing. *Prog Retin Eye Res* 22:113–133.
9. Clark RAF (1990) Fibronectin matrix deposition and fibronectin receptor expression in healing and normal skin. *J Invest Dermatol* 94:128s–134s.
10. Palecek SP, Horwitz AF, Lauffenburger DA (1999) Kinetic model for integrin-mediated adhesion release during cell migration. *Ann Biomed Eng* 27:219–235.
11. Pettit DK, Hoffman AS, Horbett TA (1994) Correlation between corneal epithelial cell outgrowth and monoclonal antibody binding to the cell binding domain of adsorbed fibronectin. *J Biomed Mater Res* 28:685–691.
12. van Horssen R, Galjart N, Rens JAP, Eggermont AMM, ten Hagen TLM (2006) Differential effects of matrix and growth factors on endothelial and fibroblast motility: Application of a modified cell migration assay. *J Cell Biochem* 99:1536–1552.
13. Aucoin L, Griffith CM, Pleizier G, Deslandes Y, Sheardown H (2002) Interactions of corneal epithelial cells and surfaces modified with cell adhesion peptide combinations. *J Biomat Sci-Polym E* 13:447–462.
14. Nowatzki PJ, Tirrell DA (2003) Physical properties of artificial extracellular matrix protein films prepared by isocyanate crosslinking. *Biomaterials* 25:1261–1267.
15. Di Zio K, Tirrell DA (2003) Mechanical properties of artificial protein matrices engineered for control of cell and tissue behavior. *Macromolecules* 36:1553–1558.
16. Heilshorn SC, Di Zio KA, Welsh ER, Tirrell DA (2003) Endothelial cell adhesion to the fibronectin CS5 domain in artificial extracellular matrix proteins. *Biomaterials* 24:4245–4252.
17. Liu JC, Heilshorn SC, Tirrell DA (2004) Comparative cell response to artificial extracellular matrix proteins containing the RGD and CS5 cell-binding domains. *Biomacromolecules* 5:497–504.
18. Liu JC, Tirrell DA (2008) Cell response to RGD density in cross-linked artificial extracellular matrix protein films. *Biomacromolecules* 9:2984–2988.
19. Lu L, Reinach PS, Kao WWY (2001) Corneal epithelial wound healing. *Exp Biol Med* 226:653–664.
20. Stepp MA (2006) Corneal integrins and their functions. *Exp Eye Res* 83:3–15.
21. Evans MDM, Steele JG (1997) Multiple attachment mechanisms of corneal epithelial cells to a polymer-cells can attach in the absence of exogenous adhesion proteins through a mechanism that requires microtubules. *Exp Cell Res* 233:88–98.
22. Evans MDM, Steele JG (1998) Polymer surface chemistry and a novel attachment mechanism in corneal epithelial cells. *J Biomed Mater Res* 40:621–630.
23. Chan KY, Patton DL, Cosgrove YT (1989) Time-lapse videomicroscopic study of in vitro wound closure in rabbit corneal cells. *Invest Opthalmol Vis Sci* 30:2488–2498.
24. Farooqui R, Fenteany G (2005) Multiple rows of cells behind an epithelial wound edge extend cryptic lamellipodia to collectively drive cell sheet movement. *J Cell Sci* 118:51–63.
25. Lauffenburger DA (1996) Cell Migration: A physically integrated molecular process. *Cell* 84:359–369.
26. Bell GI (1978) Models for specific adhesion of cells to cells. *Science* 200:618–627.
27. Weikl TR, Asfaw M, Krobath H, Rozycki B, Lipowsky R (2009) Adhesion of membranes via receptor-ligand complexes: Domain formation, binding cooperativity, and active processes. *Soft Matter* 5:3213–3224.
28. Prass M, Jacobson K, Mogilner A, Radmacher M (2006) Direct measurement of the lamellipodial protrusive force in a migrating cell. *J Cell Biol* 174:767–772.
29. Pierres A, Monnet-Corti V, Benoliel AM, Bongrand P (2009) Do membrane undulations help cells probe the world? *Trends Cell Biol* 19:428–433.
30. Zidovska A, Sackmann E (2006) Brownian motion of nucleated cell envelopes impedes adhesion. *Phys Rev Lett* 96:048103–048101–048104.
31. Kahn CR, Young E, Lee IH, Rhim JS (1993) Human corneal epithelial primary cultures and cell-lines with extended life-span—in-vitro model for ocular studies. *Invest Opthalmol Vis Sci* 34:3429–3441.
32. Fichthorn KA, Weinberg WH (1991) Theoretical foundations of dynamic monte-carlo simulations. *J Chem Phys* 95:1090–1096.
33. Kang CH, Weinberg WH (1992) Dynamic monte-carlo simulations of surface-rate processes. *Accounts Chem Res* 25:253–259.

Supporting Information

Fong et al. 10.1073/pnas.1008291107

Materials and Methods.

Human Corneal Epithelial (HCE) Cell Culture. Primary human corneal epithelial cells were obtained from ScienCell Research Laboratories and Cascade Biologics. All cells were maintained in serum-free EpiLife culture medium (with 60 μM CaCl$_2$, Cascade Biologics) supplemented with Human Corneal Growth Supplement (HCGS containing bovine pituitary extract, bovine insulin, hydrocortisone, bovine transferrin, and mouse epidermal growth factor, Cascade Biologics). Gentamicin (10 μg/ml) and amphotericin (0.25 μg/ml) were also added to culture media. Serum-free EpiLife medium was used in all experiments to exclude extracellular matrix proteins (i.e., fibronectin, laminin) present in serum. Cells in passages 2 to 7 were used.

Cell Spreading. Aliquots (500 μl) of FN and BSA solutions were added to the wells of a transparent 24-well plate (Falcon BD, VWR) and allowed to adsorb overnight at 4 ºC. In these experiments, fibronectin (FN, 10 μg/ml in PBS, Chemicon) was used as a positive control and bovine serum albumin (BSA, 2 mg/ml in PBS, Sigma) was used as a negative control. Subsequently, wells were rinsed twice with prewarmed PBS solution and blocked with 500 μl of 0.2 wt% heat-inactivated BSA solution at room temperature for 30 min. At the same time, coverslips containing spin-coated aECM protein films were mounted in empty wells by dotting sterile grease around the circumference of the coverslips. Gentle pressure was applied to ensure firm adhesion to the well. Finally, all wells were rinsed twice with prewarmed PBS solution.

HCE cells were enzymatically passaged using 0.05% Trypsin-0.25% EDTA (Cascade Biologics). To each well, 4.8×10^4 cells were added together with 1 ml of fresh EpiLife medium. The plates were swirled gently to prevent clustering of cells and placed in an incubator at 37 ºC under 5% CO$_2$/95% air. Images of five random positions in each well were acquired after 4 h. Using ImageJ, 200 cells were traced for each surface and their areas were recorded. Cells with projected areas above 300 μm^2 (based on the average cell areas on BSA), cells were considered spread and the percentage of spread cells was plotted for each surface.

Characterization of Cross-Linked aECM Films by Atomic Force Microscopy (AFM). Images and force curves were collected on an Asylum MFP-3D-BIO atomic force microscope, with accompanying IGOR Pro v.5.05 software. Pyramidal-tipped silicon nitride cantilevers (Veeco DNP-S) with nominal spring constant 0.58 N/m were used for imaging. The tip of a pair of fine forceps was drawn lightly across the surface of the protein film, prepared as described above, tearing away the protein along the scratch and exposing the underlying glass substrate. The edge of the scratch was imaged by AFM both dry and in water, and the thickness of the film was determined. Scans were made at various positions along the scratch to obtain an average measurement. The average film thickness was calculated by averaging the height measurements obtained from 5 positions, using the revealed glass as a baseline. Thicknesses measured on three separate films were averaged.

For nanoindentation studies, tips with 600 nm SiO$_2$ microspheres attached at the tip end (Novascan Technologies) were used (1). Protein films with predetermined thicknesses were immersed in water for at least 1 h at room temperature to allow equilibrium water uptake. Both the films and the cantilever assembly were submerged in water under ambient conditions during nanoindentation. Force curves were collected; the instrument

records z (piezo) displacement and force, the product of measured tip deflection and cantilever spring constant. The maximum indentation force was set to 50 nN relative to the contact point. The tip speed was 1 μm/ sec, and data were collected at 0.5 Hz.

The spring constants of the tips used for nanoindentation were determined to be about 0.3 N/m using thermal calibration in water. The Dimitriadis model (2) for indentation of linear-elastic soft material films of finite height with a spherical indenter was applied to the loading force data. Only force-indentation points between 20 nm and 10% maximum indentation were used to constrain the data to the near-linear response range. The elastic modulus was obtained by averaging the calculated moduli at multiple points in three separate films.

Dehydrated films were determined to be in the range of 193 ± 19 nm ($n = 70$) in thickness; hydrated films were 349 ± 26 nm ($n = 36$) thick. Based on measured height differences, water content in hydrated films was estimated to be approximately 45%. The elastic modulus of a hydrated film was determined to be 0.24 ± 0.06 MPa ($n = 21$), which falls within the range previously determined for films of similar aECM proteins (1). There were no discernible physical differences among films with varying RGD concentrations.

A typical surface used for studying the crossing probabilities was imaged by AFM (Fig. S2). The height of the step at the boundary was 119 ± 14 nm ($n = 30$).

Estimation of RGD Surface Density. The surface density of RGD domains in each film was estimated by assuming a density of elastin of 1.32 g/cm^3, a protein weight fraction of 0.45 (determined by comparing wet and dry films by AFM), and an accessible surface depth of 10 nm.

Extracting Simulation Parameters from Single Cell Spreading Data. As explained in *Materials and Methods* (Eq. **9**), the connection between the spreading and retraction rates on surfaces with the same RGD fraction, φ_{RGD}, is

$$\tilde{W}_r(\varphi_{\mathrm{RGD}}) = \exp(f'\gamma'/k_{\mathrm{B}}T)[A - \tilde{W}_s(\varphi_{\mathrm{RGD}})]$$
$$- k \exp(-\varepsilon_{\mathrm{el}}/k_{\mathrm{B}}T)/W_s(FN) \qquad [\text{S1}]$$

where $A \equiv k \exp(-\varepsilon_{\mathrm{el}}/k_{\mathrm{B}}T + f\gamma/k_{\mathrm{B}}T)/W_s(FN)$. If we assume that the binding energy, ε is proportional to the RGD fraction on the surface, i.e., $\varepsilon = \tilde{\varepsilon}\varphi_{\mathrm{RGD}}$, we get

$$\tilde{W}_s = A - B \exp(-\tilde{\varepsilon}\varphi_{\mathrm{RGD}}/k_{\mathrm{B}}T) \qquad [\text{S2}]$$

where $B \equiv k/W_s(FN)$.

The percent spread cells on aECM with different RGD concentrations after 4 h (shown in Fig. 1*E*) relative to the percent of spread cells on FN after 4 h, was taken as a measure for the relative rate of cell spreading, $\tilde{W}_s$ and was fitted to Eq. **S2**. Out of the fit we obtain $A = 1.11$. The fit is shown in Fig. S3.

Derivation of an Expression for the Proliferation Rate. The number of cells confined to a single lattice site is denoted by n_1 (red circle, Fig. S4); the number of spread on two adjacent lattice sites by n_2 (red oval, Fig. S4). The empty square in Fig. S4 represents an empty neighboring site on the lattice. The rates for spreading, retraction and proliferation steps are denoted by W_s, W_r, and W_p, respectively.

In our model, only cells that are spread on two adjacent lattice sites can proliferate. This assumption is consistent with the observation that decreased cell spreading can inhibit proliferation signals (3), and it creates an effective time lag between consecutive cell divisions, resembling interphase (4).

The rate equations for the kinetic scheme illustrated in Fig. S4 are

$$\frac{dn_1}{dt} = -W_s n_1 (1 - n_1/n_1^* - n_2/n_2^*) + W_r n_2 + 2W_p n_2 \qquad [\text{S3}]$$

$$\frac{dn_2}{dt} = W_s n_1 (1 - n_1/n_1^* - n_2/n_2^*) - W_r n_2 - W_p n_2. \qquad [\text{S4}]$$

The first term is the rate of spreading, where the probability to find a neighboring empty lattice site is taken to be the mean field probability, i.e., $P_{\text{empty}_{\text{site}}} = (1 - \theta)$ where θ is the fraction of occupied sites on the lattice and is given by $\theta = n_1/n_1^* + n_2/n_2^*$ where n_1^* is the number of cells that occupy a single site when at confluence. Likewise, n_2^* is the number of cells that occupy two adjacent sites at confluence.

The change in the total number of cells $n = n_1 + n_2$ is then

$$\frac{dn}{dt} = \frac{dn_1}{dt} + \frac{dn_2}{dt} = W_p n_2. \qquad [\text{S5}]$$

Since for most cases, $W_p \ll W_r, W_s$, we can assume fast equilibrium in order to solve the rate equations (Eqs. S3 and S4). In the limit of low cell concentration ($n_1/n_1^* \ll 1$), we get the expected exponential growth

$$\frac{dn}{dt} = \frac{W_p}{1 + \left(\frac{W_r}{W_s}\right)} n. \qquad [\text{S6}]$$

The doubling time, t_D, for a cell population which grows according to the kinetic scheme presented in Fig. S4 is

$$t_D = \frac{\ln 2}{W_p} (1 + W_r/W_s). \qquad [\text{S7}]$$

According to the literature, the doubling time for human corneal epithelial (HCE) cells is estimated to be 25 h (5). Using the values for W_r and W_s on FN, we get $W_p = 0.05$ h^{-1}. We assume that W_p is identical on all the surfaces. We find that this treatment overestimates the contribution of proliferation to wound healing, but that the calculated variation in proliferation rates from surface to surface is modest, as observed experimentally (Fig. S7 B and C).

Including Cell–Cell Interactions in the Simulation. Wound-healing behavior depends not only on cell-aECM interaction but also on intercellular interaction. The energy of a cell fluctuates, but unlike in a fluid, the origin of the fluctuations is not collisions with the solvent or the thermal energy. The fluctuations in energy in a cellular system originate from fluctuations around the steady state of the biochemical networks of the cell (6). Consequently, it is accepted to define an effective temperature $T_{\text{eff}} = F_T/k_B$ where F_T is the magnitude of the energy fluctuations and k_B is the Boltzmann constant (7–9). As a result, the probability of a cell to have an energy fluctuation ε' is $\exp(-\varepsilon'/F_T)$.

In the simulation, we measure the intercellular interaction energy between nearest neighbor cells, $\varepsilon_{\text{cell-cell}}$, in units of F_T. The interaction energy between cells comes into play in the simulation for the case of cell retraction. When a cell retracts, there is an active force that pulls it from the surface and from its neighbors as explained in the model for spreading and retraction (see *Materials and Methods*). This force can either lead to cell–cell bond breakage or to retraction of the cell, pulling the neighboring cell along.

Let us denote the number of neighbors that the cell in question would lose upon retraction by v. The cell can retract and break the bonds with its neighbors with a probability $W_r \times (\exp(-\varepsilon_{\text{cell-cell}}/F_T))^v$. Alternatively, the cell can retract, break the bonds with $v - 1$ of its neighbors and pull the remaining cell with it with probability $W_r \times (\exp(-\varepsilon_{\text{cell-cell}}/F_T))^{v-1}$. A neighboring cell can only be stretched if it occupies a single lattice site. This is to ensure that the total elastic energy of the cell does not exceed the cell fluctuation energy F_T.

HCE cells are characterized by relatively weak cell–cell contacts and behave much like a weakly interacting liquid. We quantified the dynamic behavior of the cell sheet by measuring experimentally the average cell–cell bond survival time. The average bond survival time was 1.64 ± 0.24 hours. Fig. S5 shows the dependence of the average bond survival time in the simulation on the interaction energy. The interaction energy value that best mimics the behavior observed experimentally is $\varepsilon_{\text{cell-cell}}/F_T = 0.7$.

Single Cell Crossing Rates. When a cell is at the boundary, it can either cross the boundary with a rate constant, k_c or move away from the boundary with a rate constant, k_b as illustrated in the schematic in Fig. S6A.

From the time-lapse movies, we recorded the time spent by the cell at the boundary until a reaction occurs (i.e., waiting time), as well as the outcome (i.e., crossing or moving away). In order to extract the rate constant for boundary crossing from the experiment, it is necessary to know the waiting time distribution for cells at the boundary.

Let us define $P_0(t; t_0)$ as the probability that no event occurs in the interval $(t_0, t_0 + t)$ and assume that the events are independent and the rate constants do not depend on time. Then, $P_0(t + dt; t_0) = P_0(t; t_0) \times (1 - \sum_i k_i dt)$, where k_i is the rate constant for event i (in our case: $i = c, b$).

Consequently, $\frac{P_0(t+dt;t_0)-P_0(t;t_0)}{dt} = (-\sum_i k_i)P_0(t;t_0)$.

And in the limit of $dt \to 0$, we get: $\frac{dP_0(t)}{dt} = (-\sum_i k_i)P_0(t)$ so that $P_0(t) = \exp(-\sum_i k_i \times t)$.

We denote the waiting time distribution as $w(t)$. The waiting time distribution can be expressed as $w(t) = (P_0(t) - P_0(t + dt))/dt = -dP_0(t)/dt$ and hence,

$$w(t) = K \exp(-Kt) \qquad [\text{S8}]$$

where $K = \sum_i k_i$ is the sum of the rate constants for all possible events.

Using the waiting time distribution (Eq. S8), the average waiting time is

$$\langle t \rangle = \frac{\int_0^\infty t \times K \exp(-Kt)dt}{\int_0^\infty K \exp(-Kt)dt} = \frac{1}{K}. \qquad [\text{S9}]$$

In the case of the cell crossing experiment, the waiting at the boundary can end with either crossing of the boundary (k_c) or with moving away from the boundary (k_b). Thus, the average waiting time becomes: $\langle t \rangle = 1/(k_c + k_b)$.

If we define N_c as the number of events which end with boundary crossing and N as the total number of events, we get

$$\frac{N_c}{N} = \frac{k_c}{k_c + k_b}. \qquad [10]$$

Using Eqs. S8–S10, the rate constant of boundary-crossing can be expressed as

$$k_c = \frac{N_c}{N\langle t \rangle}. \qquad [\text{S11}]$$

Notice that according to Eq. S11, the rate constant of boundary crossing, k_c, can be calculated as the number of crossing events divided by the total waiting time at the boundary, $t_{\text{total}} = N\langle t \rangle$.

1. Nowatzki PJ, Tirrell DA (2003) Physical properties of artificial extracellular matrix protein films prepared by isocyanate crosslinking. *Biomaterials* (25):1261–1267.
2. Dimitriadis EK, Horkay F, Maresca J, Kachar B, Chadwick RS (2002) Determination of elastic moduli of thin layers of soft materials using the atomic force microscope. *Biophys J* 82:2798–2810.
3. Nelson CM, Chen CS (2002) Cell-cell signaling by direct contact increases cell proliferation via a PI3K-dependent signal. *FEBS Lett* 514:238–242.
4. Alberts B et al. (2008) *Molecular Biology of the Cell* (Garland Science, New York) pp 637–655.
5. Kahn CR, Young E, Lee IH, Rhim JS (1993) Human corneal epithelial primary cultures and cell-lines with extended life-span—in-vitro model for ocular studies. *Invest Opthalmol Vis Sci* 34:3429–3441.
6. Goodwin BC (1963) *Temporal Organization in Cells: A Dynamic Theory of Cellular Control Processes* (Academic Press, New York) pp 55–80.
7. Beysens DA, Forgacs G, Glazier JA (2000) Cell sorting is analogous to phase ordering in fluids. *Proc Natl Acad Sci USA* 97:9467–9471.
8. Neagu A, Jakab K, Jamison R, Forgacs G (2005) Role of physical mechanisms in biological self-organization. *Phys Rev Lett* 95:178101–178104.
9. Drasdo D, Hohme S (2005) A single-cell-based model of tumor growth in vitro: Monolayers and spheroids. *Phys Biol* 2:133–147.

aECM-RGD:

M-MASMTGGQQMG-HHHHHHH-DDDDK(LD-YAVTG**RGD**SPASSKIA((VPGIG)$_2$VPG*K*G(VPGIG)$_2$)$_4$VP)$_3$-LE

T7 tag   His tag   Cleavage site   RGD cell-binding domain   Elastin-like domain

aECM-RDG:

M-MASMTGGQQMG-HHHHHHH-DDDDK(LD-YAVTG**RDG**SPASSKIA((VPGIG)$_2$VPG*K*G(VPGIG)$_2$)$_4$VP)$_3$-LE

Scrambled RGD cell-binding domain

Fig. S1. Amino acid sequences of aECM proteins containing RGD and RDG cell-binding domains. Each aECM protein contained a T7 tag, a hexahistidine tag, an enterokinase cleavage site, and elastin-like domains containing lysine residues (italicized) for cross-linking.
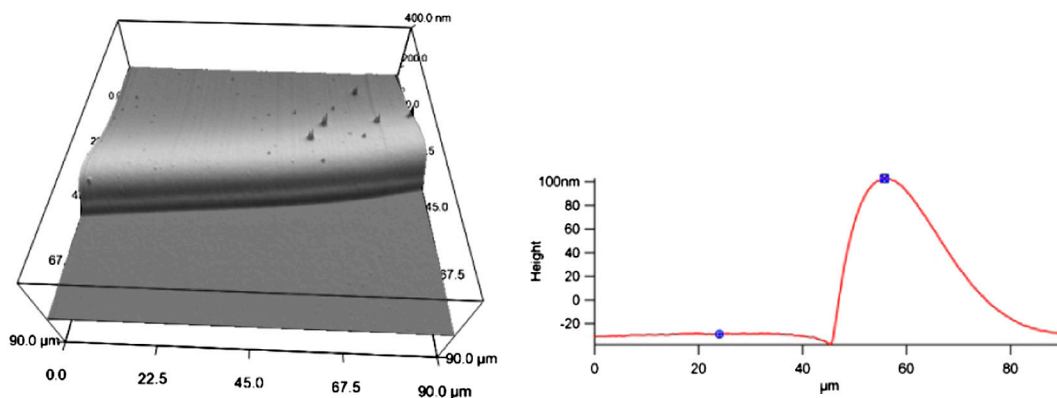
Fig. S2. Image of typical substrate with a boundary imaged by atomic force microscopy (left). A cross-section of the boundary region is also shown (right).
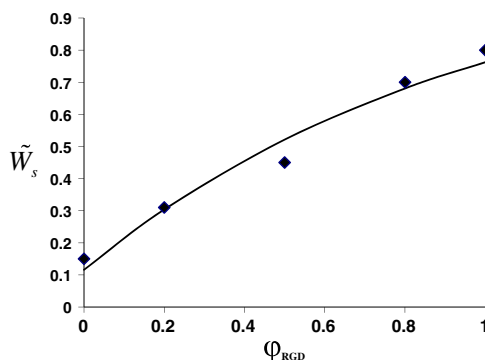
Fig. S3. The fit of the experimental spreading data to the theoretical expression for the relative spreading rate, Eq. **S2**.
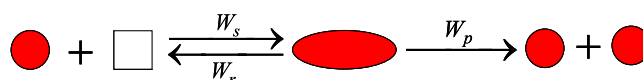
Fig. S4. An illustration of the proliferation kinetic scheme. The white box represents an empty neighboring lattice site on which the cell can spread in order to proliferate.

Fig. S5. The average bond survival time as a function of the cell–cell interaction energy in the simulation.

Fig. S6. (*A*) Schematic diagram of cell at a boundary, showing two possible outcomes. A cell can cross the boundary with a rate constant k_c, or it can move away with a rate constant, k_b. (*B*) Rate constants of boundary crossing, k_c, from 100% RGD into various test surfaces. The crossing probabilities computed for both configurations of the boundary. There were no significant differences between the rate constants for the two configurations of each test surface, suggesting that the small "step" at the boundary did not affect the boundary-crossing rate. (*C*) Rate constants of boundary crossing from FN to test surfaces obtained from simulation. The crossing rates from 100% RGD to 100% RGD and from 100% RGD to 2.5% RGD differ by a factor of five, consistent with experimental observations (Table S1).

Fig. S7. Contributions to wound closure. (*A*) Comparison of average cell speeds for the first and last 10-h periods after wounding. (*B*) Proliferation on the test surface and in the interfacial region in the experiment. (*C*) Proliferation on the test surface and in the interfacial region in the simulation. (*D*) Numbers of cells in the wound area at $t = 30$ h that crossed the boundary during the experiment. (*E*) Numbers of cells in the wound area at $t = 30$ h that crossed the boundary in the simulation. Numbers are reported in (*D*) and (*E*) for a boundary length equal to 15 cell diameters. See Table S2 for definitions of symbols and raw data.

Movie S1. Epithelial wound healing on 2.5% RGD.

Movie S1 (AVI)

Movie S2. Epithelial wound healing on 100% RGD.

Movie S2 (AVI)

Movie S3. Simulation of wound healing on 2.5% RGD.

Movie S3 (AVI)

Movie S4. Simulation of wound healing on 100% RGD.

Movie S4 (AVI)

Movie S5. Single cell boundary crossing from 100% RGD to 100% RGD.

Movie S5 (AVI)

Movie S6. Single cell boundary crossing from 100% RGD to 0% RGD.

Movie S6 (AVI)

Table S1. Summary of the rates for 100% and 2.5% RGD surfaces

	Simulation	Experiment
Surface composition (the line represents the wound edge at time $t = 0$)	FN|RGD	FN|RGD
Wound-closure rate (μm/h) (100% RGD)	9.4	9.6
Wound-closure rate (μm/h) (2.5% RGD)	1.7	1.7
Wound-closure rate ratio (100% RGD/2.5% RGD)	5.6	5.6
Single cell speed ratio (100% RGD/2.5% RGD)	1.9	1.4

Table S2. Experimental numbers of cells and proliferation events on the test surface and in the interfacial region

	Sample #	N_{test}^{cell}	N_{test}^{p}	$N_{test}^{cell} - N_{test}^{p}$	$\frac{N_{test}^{p}}{N_{test}^{cell}}$	N_{I}^{cell}	N_{I}^{p}	$\frac{N_{I}^{p}}{N_{I}^{cell}}$	$\frac{(N_{test}^{p}+N_{I}^{p})}{(N_{test}^{cell}+N_{I}^{cell})}$
100% RGD	1	34	1	33	0.029	31	4	0.129	0.077
	2	51	3	48	0.059	30	0	0.000	0.037
	3	65	5	60	0.077	27	5	0.185	0.109
	4	60	7	53	0.117	42	8	0.190	0.147
	5	46	5	41	0.109	32	1	0.031	0.077
	6	52	4	48	0.077	33	5	0.152	0.106
	7	72	16	56	0.222	30	11	0.367	0.265
	8	71	18	53	0.254	35	13	0.371	0.292
	9	34	1	33	0.029	13	0	0.000	0.021
	10	59	8	51	0.136	29	4	0.138	0.136
	11	120	22	98	0.183	26	5	0.192	0.185
	12	120	7	113	0.058	36	5	0.139	0.077
100% RGD	Mean	65.33	8.08	57.3	0.112	30.33	5.08	0.158	0.127
	SEM	7.84	1.9	6.7	0.020	1.923	1.11	0.033	0.023
80% RGD	1	20	4	16	0.200	18	4	0.222	0.211
	2	20	1	19	0.050	20	5	0.250	0.150
	3	28	4	24	0.143	13	0	0.000	0.098
	4	98	15	83	0.153	18	4	0.222	0.164
	5	68	10	58	0.147	17	2	0.118	0.141
	6	101	16	85	0.158	23	3	0.130	0.153
	7	90	16	74	0.178	35	8	0.229	0.192
80% RGD	Mean	60.7	9.43	51.3	0.147	20.57	3.714	0.167	0.158
	SEM	13.02	2.25	10.8	0.017	2.46	0.874	0.031	0.0127
50% RGD	1	31	2	29	0.065	32	2	0.063	0.063
	2	46	6	40	0.130	23	4	0.174	0.145
	3	50	4	46	0.080	23	0	0.000	0.055
	4	60	7	53	0.117	17	2	0.118	0.117
	5	64	4	60	0.063	24	3	0.125	0.080
50% RGD	Mean	50.2	4.6	45.6	0.09082	23.8	2.2	0.0958	0.092
	SEM	5.19	0.78	4.77	0.012	2.14	0.593	0.0266	0.015
20% RGD	1	32	9	23	0.281	41	13	0.317	0.301
	2	28	3	25	0.107	23	2	0.087	0.098
	3	26	3	23	0.115	25	3	0.120	0.118
	4	24	2	22	0.083	23	3	0.130	0.106
	5	24	5	19	0.208	31	3	0.097	0.145
	6	28	3	25	0.107	24	3	0.125	0.115
20% RGD	Mean	27	4.17	22.8	0.150	27.833	4.5	0.146	0.147
	SEM	1.13	0.96	0.83	0.029	2.65	1.56	0.032	0.029
2.5% RGD	1	9	0	9	0.000	23	4	0.174	0.125
	2	30	4	26	0.133	40	11	0.275	0.214
	3	12	0	12	0.000	21	3	0.143	0.091
	4	5	0	5	0.000	21	2	0.095	0.077
	5	15	2	13	0.133	25	3	0.120	0.125
	6	8	0	8	0.000	31	4	0.129	0.103
	7	23	2	21	0.087	20	3	0.150	0.116
	8	13	1	12	0.077	36	6	0.167	0.143
2.5% RGD	Mean	14.34	1.13	13.3	0.054	27.13	4.5	0.157	0.124
	SEM	2.75	0.48	2.3	0.02	2.52	0.95	0.018	0.014

The interfacial region is defined as a region one spread-cell diameter (130 µm) deep next to the interface on the cell-sheet side (outside the wound). N_{test}^{cell} and N_{I}^{cell} denote the numbers of cells on the test surface and in the interfacial region, respectively, after 30 h. N_{test}^{p} and N_{I}^{p} denote the numbers of proliferation events on the test surface and in the interfacial region, respectively, during a 30-h period. Each sample corresponds to analysis of a separate movie of a wound-healing experiment.